HST WFC3 Early Release Science: Emission–Line Galaxies from IR Grism Observations

A. N. Straughn[1,2], H. Kuntschner[3], M. Küemmel[3], J. R. Walsh[3], S. H. Cohen[4], J.P. Gardner[2], R. A. Windhorst[4], R. W. O'Connell[5], N. Pirzkal[6], G. Meurer[7], P.J. McCarthy[8], N. P. Hathi[9], S. Malhotra[4], J. Rhoads[4], B. Balick[9], H. E. Bond[6], D. Calzetti[10], M. J. Disney[11], M. A. Dopita[12], J. A. Frogel[13], D. N. B. Hall[14], J. A. Holtzman[15], R. A. Kimble[2], G. Luppino[14], F. Paresce[16], A. Saha[17], J. I. Silk[18], J. T. Trauger[19], A. R. Walker[20], B. C. Whitmore[6], and E. T. Young[21]

[1]amber.n.straughn@nasa.gov

[2]Astrophysics Science Division, Goddard Space Flight Center, Code 665, Greenbelt, MD 20771

[3]Space Telescope European Coordinating Facility, Karl Schwarzschild Str. 2, D 85748 Garching, Germany

[4]School of Earth and Space Exploration, Arizona State University, Tempe, AZ 85287

[5]Department of Astronomy, University of Virginia, Charlottesville, VA 22904-4325

[6]Space Telescope Science Institute, Baltimore, MD 21218

[7]International Centre for Radio Astronomy Research, The University of Western Australia, Crawley WA, 6009

[8]Observatories of the Carnegie Institute of Washington, Pasadena, CA 91101

[9]Department of Physics & Astronomy, University of California, Riverside, CA 92521

[9]Department of Astronomy, University of Washington, Seattle, WA 98195-1580

[10]Department of Astronomy, University of Massachusetts, Amherst, MA 01003

[11]School of Physics and Astronomy, Cardiff University, Cardiff CF24 3AA, United Kingdom

[12]Research School of Astronomy & Astrophysics, The Australian National University, ACT 2611, Australia

[13]Association of Universities for Research in Astronomy, Washington, DC 20005

[14]Institute for Astronomy, University of Hawaii, Honolulu, HI 96822

[15]Department of Astronomy, New Mexico State University, Las Cruces, NM 88003

[16]European Southern Observatory, Garching bei München, 85748 Germany

[17]National Optical Astronomy Observatories, Tucson, AZ 85726-6732

[18]Department of Physics, University of Oxford, Oxford OX1 3PU, United Kingdom

[19]NASA–Jet Propulsion Laboratory, Pasadena, CA 91109

[20]Cerro Tololo Inter-American Observatory, La Serena, Chile

[21]NASA–Ames Research Center, Moffett Field, CA 94035

ABSTRACT

We present grism spectra of emission–line galaxies (ELGs) from 0.6–1.6 microns from the Wide Field Camera 3 (WFC3) on the Hubble Space Telescope (HST). These new infrared grism data augment previous optical Advanced Camera for Surveys G800L (0.6–0.95 micron) grism data in GOODS–South, extending the wavelength covereage well past the G800L red cutoff. The ERS grism field was observed at a depth of 2 orbits per grism, yielding spectra of hundreds of faint objects, a subset of which are presented here. ELGs are studied via the Hα, [O III], and [O II] emission lines detected in the redshift ranges $0.2\lesssim z\lesssim 1.6$, $1.2\lesssim z\lesssim 2.4$ and $2.0\lesssim z\lesssim 3.6$ respectively in the G102 (0.8–1.1 microns; R$\sim$210) and G141 (1.1–1.6 microns; R$\sim$130) grisms. The higher spectral resolution afforded by the WFC3 grisms also reveals emission lines not detectable with the G800L grism (e.g., [S II] and [S III] lines). From these relatively shallow observations, line luminosities, star–formation rates, and grism spectroscopic redshifts are determined for a total of 25 ELGs to $m_{AB(F098M)}\sim 25$ mag. The faintest source in our sample—with a strong but unidentified emission–line—is $m_{AB(F098M)}=26.9$ mag. We also detect the expected trend of lower specific star formation rates for the highest mass galaxies in the sample, indicative of downsizing and discovered previously from large surveys. These results demonstrate the remarkable efficiency and capability of the WFC3 NIR grisms for measuring galaxy properties to faint magnitudes.

Subject headings: catalogs — techniques: spectroscopic — galaxies: starburst

1. Introduction

Galaxies that are actively forming stars make up a distinct population of sources that are involved in ongoing evolution—that is, they are in the very process of converting gas into stars and thereby changing their chemical content. Star–forming galaxies are also often associated with larger scale galaxy evolution, in that galaxy interactions are often found to cause enhanced star formation (Li et al. 2008, Overzier et al. (2008), Larson & Tinsley (1978)) and galaxy evolution as a whole is thought to proceed hierarchically via galaxy interactions and merging (White & Frenk 1991; Navarro et al. 1997). These galaxies are thus important to study within the overall context of galaxy assembly. Information about star formation activity is revealed in the galaxies' emission lines, particularly Hα, [O III], and [O II] at rest–frame wavelengths λ6563Å, $\lambda\lambda$4959Å, 5007Å, and λ3727Å respectively. Many

studies have used emission lines to investigate the star–forming properties of galaxies over various redshift ranges (Hammer et al. 1997; Kennicutt 1983; Gallego et al. 1995; Kewley et al. 2004; NICMOS grism study: McCarthy et al. 1999; Yan et al. 1999).

The installation of the new Wide Field Camera 3 (WFC3) on the Hubble Space Telescope (HST) in mid–2009 has provided a new capability for studying star formation and has already resulted in a variety of scientific discoveries in observational cosmology. Particularly, the increase in sensitivity, field of view, and resolution of the WFC3/IR over previous infrared instrumentation has been used to detect some candidates for the most distant galaxies ever observed (Bouwens et al. 2010, Yan et al. 2010, Oesch et al. 2010, McLure et al. 2010, etc.) from the ultra–deep WFC3 imaging (Illingworth et al. PID GO–11563) of the Hubble Ultra Deep Field (HUDF; Beckwith et al. 2006). The less deep but wider–area broadband data from the Early Release Science (ERS) II (PI O'Connell, PID GO–11359) program have also been used to study high–redshift candidates (Wilkins et al. 2010, Yan et al. 2010). Windhorst et al. 2010 (in preparation) will describe the WFC3 ERS data in detail, and other studies based on these data are forthcoming.

In addition to the broadband data used for most of these studies, the ERS II program also consists of one field observed with both the G102 (0.8–1.1 microns; R$\sim$210) and G141 (1.1–1.6 microns; R$\sim$130) infrared grisms (described in detail below). van Dokkum et al. (2010) report on a bright z=1.9 compact galaxy in the ERS grism data. Here, we present emission–line galaxies from the WFC3 ERS grism observations, demonstrating the unique capability of this instrument for detecting star–forming galaxies in the infrared reaching to magnitudes $m_{AB(F098M)}\sim25$ with only 2 orbits of HST time. By searching for star–formation in the infrared grism data, we are able to push detection of these galaxies and subsequent measurement of their physical properties to redshifts z$\sim$2.0. Grism studies with HST's Advanced Camera for Surveys (ACS) G800L grism have proven efficient at detecting emission–line galaxies (ELGs) in the optical (Straughn et al. 2008, Straughn et al. 2009, Xu et al. 2007, Pirzkal et al. 2006), and here we extend these studies of ELGs to the infrared.

2. Data

The ERS II program for WFC3 consists of both UV and IR observations of about 30% of the GOODS–South field (Giavalisco et al. 2004). Here we summarize the ERS II program; Windhorst et al. (2010, in preparation) present the ERS II data reduction effort in detail. Eight pointings were imaged with the UVIS channel (broadband filters F225W, F275W, and F336W at depths of 2 orbits/field/filter for F225W and F275W and 1 orbit/field/filter for F336W) and ten with the IR channel (broadband filters F098M, F125W, F160W) at 2

orbits/field/filter. Grism observations of one WFC3 pointing (c.f. Fig. 1) were performed using the infrared "blue" G102 grism (R$\sim$ 210) and the "red" (R$\sim$130) G141 grism, providing spectral coverage from 0.8–1.6 microns at 2 orbits/grism depth.

The WFC3 IR channel has a field of view of 123 x 136 arcsec at a resolution of 0.19 arcsec/pixel. The ten WFC3/ERS II IR fields span the northern $\sim$40 square arcminutes of GOODS–South, providing new high–resolution infrared imaging to accompany this widely–used multiwavelength dataset. The ERS II grism field lies in the north–central region of the ERS II imaging field (Fig. 1; J2000 53.071121 -27.709646) and is overlapped completely by the HST Probing Evolution And Reionization Spectroscopically (PEARS; Malhotra PID 10530) ACS grism survey South Field #4. As such, combined with the earlier ACS data, these new infrared grism data provide unprecedented spectral grism coverage in the optical to infrared wavelength range of objects reaching to continuum magnitude $m_{AB(F098M)}\sim$25.

3. Analysis

The latest version (December 1, 2009) STSDAS *calwf3* pipeline reduced direct imaging and the associated grism exposures were obtained from the MAST Archive. The direct images were combined for each of the F098M and F140W filters using Multidrizzle (Koekemoer et al. 2002). Source catalogues were produced for each filter using SExtractor (Bertin & Arnouts). The resulting catalogues were cleaned to remove spurious sources at the edges and artifacts from persistence effects caused by a bright star in the preceding ERS grism observations. The faintest detected source was AB magnitude 25.4 and 26.0 for the F098M and F140W filters respectively.

The final, cleaned source catalogues were used with the aXe grism reduction software (version 2.0; Kümmel et al. 2009) to extract a calibrated 2–dimensional, co–added grism spectrum for each source. Master sky backgrounds for each grism were constructed from all publicly available grism data as of February 2010 and subtracted from the ERS observations prior to spectral reduction. The final 2–dimensional grism spectra include information about the associated errors and contamination by spectra of neighboring objects. The trace and wavelength calibration used by aXe to extract the spectra was based on the first in–orbit calibration observations (Kuntschner et al. 2009a,b).

3.1. Source Selection

We examined all PEARS sources located in the ERS grism field; many ELGs with prominent emission lines detected in PEARS with the G800L grism also have lines in the infrared. In addition to previously–detected PEARS ELGs, there are also sources in the field in which the strongest emission lines lie exclusively in the infrared and so were not detected in PEARS. We used standard Gaussian fitting techniques to measure emission line fluxes and calculate SFRs based on the line luminosities, as described in the following Section. ELGs that have line flux measurements with S/N$\gtrsim$2 are retained in the final catalog (Table 1). Whereas the PEARS pre–selected galaxies by definition have more than one line—and therefore line identifications are unambiguous and in most cases already determined by the ACS grism spectra—a small number of ERS II ELG candidates only have one emission line identified. For these sources, spectroscopic and photometric redshift catalogs (Grazian et al. 2006; Wuyts et al. 2008) are consulted in order to determine if the source has a previously–measured redshift. If it does, line identification is accomplished via this redshift and a grism–spectroscopic redshift is calculated based on the line identification. If it does not, the line remains unidentified (see Table 1; one source). However, the majority of the ELGs have two or more emission lines, and therefore it is straightforward to assign line identifications based on the emission line wavelength ratio. The fraction of objects with two lines in the spectra is considerably higher than in the PEARS studies (where the fraction of sources with two lines was ~30%) for two main reasons. First, the wavelenth range for both the G102 and G141 is longer by a factor of more than 2; and second, the higher spectral resolution afforded by both WFC3 grisms allows detection of lines not previously seen in the G800L observations; namely, [S II]$\lambda\lambda$6716+6731Å is now sufficiently resolved from Hα (Figure 2) and [S III]$\lambda\lambda$9069, 9532 Å is detected in several sources as well.

4. Results

4.1. ACS + WFC3 ELGs

A total of 25 PEARS–detected ELGs fall into the ERS II grism field, and 13 of these have emission lines in the G102/G141 bandpasses with fluxes having S/N$\gtrsim$2; these are given in Table 1. Many of these objects are sources with [O III] emission in the optical, with Hα falling in the G102 grism bandpass. One such example is Object # 370 (PEARS Object # 119489; Straughn et al. 2009). This object is also a CDF–S X–ray source (Grogin et al. 2007), which was observed to have one strong line in the optical. We now observe another strong line in the infrared, making line identifications possible (Figure 2). For this galaxy, [O III] is observed

in the optical and Hα (as well as [S II] and [S III]) in the infrared. Several PEARS–detected galaxies have [O III] emission near the red edge of the G800L bandpass, which overlaps with the G102 grism, and so [O III] is observed in G102 as well. For these sources, Hα falls into the lower–resolution G141 bandpass. Several other single–line PEARS ELGs also have emission lines detected in G102 and/or G141 and now have grism–spectroscopic redshifts, thus demonstrating the utility of the extended wavelength/redshift range compared to ACS G800L for identifying emission lines. Due to the higher resolution of the G102 grism, the [O III] $\lambda\lambda$4959Å, 5007Å lines are resolved in these data (e.g., Fig. 2 middle panel), whereas they are blended in the ACS G800L grism data. Also of note in this sample are the sources which have prominent emission lines in all three grism bandpasses—and thus different star–formation indicators which we investigate below.

4.2. New WFC3–Only ELGs

In addition to PEARS ELGs, other emission line sources were identified in the ERS II grism field that do not have lines detected in the optical grism data. These ELG candidates were fit with Gaussian profiles as described above, and 12 sources that make the S/N$\gtrsim$2 cut are listed in Table 1. These WFC3 ERS II ELGs have an average continuum magnitude of $m_{AB(F098M)}$=22.8 mag, with the faintest source detected $m_{AB(F098M)}$=26.9. Prevalent among these objects are ELGs with Hα in the G102 bandpass; many of these also have [S III] detections in G141 (Fig. 3). A few of the WFC3–detected sources are z$\gtrsim$1 galaxies with [O II] and/or [O III] lines visible in the IR grism bandpasses (e.g., Objects 242 and 262 in Table 1). Grism redshifts (Fig. 5) are derived for all sources as described in Section 3.2 and are also presented in Table 1.

4.3. Star–Formation in ERS II ELGs

The longer wavelength range over which to detect emission lines provides more sources with multiple lines that can be used in calculating SFRs. In particular, Hα —the emission line which yields the most direct and secure SFR estimate (e.g., Kennicutt 1998)—is now observed in 20 sources. For each of the ELGs, we calculate SFRs via the prescription of Kennicutt 1998 for Hα and [O II]. Using the [O III] line to arrive at a SFR is less secure due to the effects of metallicity and gas temperature (Kennicutt et al. 2000, Kennicutt 1992). For four of the ELGs in the sample, [O III] is the only line measured in the spectrum, and thus we use the [O III] SFR calibration from Straughn et al. (2009), which is derived from ELGs with both Hα and [O III] in their spectra, and should be considered a lower limit.

Figure 6 shows the SFR as a function of redshift for these galaxies, using Hα when available; then [O II] and [O III] in order of preference. The detection limit is evident in this plot; we see the expected bias toward higher SFRs at higher redshifts.

We also compare the SFRs calculated via emission lines to those from spectral energy distribution (SED) fits to the broadband photometry (Cohen et al. 2010, in prep.). As expected, the largest scatter occurs when the indicator is the less–reliable [O III] or [O II]. However, SFRs derived from emission line fluxes and those from SED fits probe different aspects of the galaxies' physical properties. In particular, SFR_{EL} gives the instantaneous rate of newly forming massive stars, as the Hα flux arises directly from ionizing photons from O stars. The SFR_{SED} approximates time–averaged star–forming activity in the galaxies. Investigation of the ratio of SFR_{EL}:SFR_{SED} therefore tentatively provides insight into a galaxy's instantaneous observed–frame star formation activity as compared to the galaxy's star–forming activity over its lifetime. The ELGs with the lowest SFR_{EL}:SFR_{SED} ratios generally have redder (rest–frame) colors, while the highest SFR_{EL}:SFR_{SED} ratio ELGs are bluer and more compact, which is expected for more actively star–forming systems.

The specific star–formation rates (sSFRs; SFR per unit mass) of these galaxies are shown as a function of stellar mass in Figure 7, which agrees with the general negative trend observed previously for galaxies at redshifts up to z$\sim$2 (e.g., Elbaz et al. 2007, Daddi et al. 2007, Noeske et al. 2007, Erb et al. 2006, Rodighiero et al. 2010, etc.). In Figure 8 we show the sSFR as a function of redshift in different mass bins, which roughly follows the expected trends of lower sSFR for higher mass galaxies (e.g., Zheng et al. 2007, Damen et al. 2009, Rodighiero et al. 2010). While previous studies investigating the sSFR as a function of redshift have made use of very large samples of galaxies from an array of large observational programs (COMBO–17, Zheng et al. 2007; SIMPLE—Spitzer IRAC and MUSYC, Fazio et al. 2004, Damen et al. 2009; GOODS, Dickenson et al. 2003; see also Martin et al. 2007 and Perez–Gonzalez et al. 2008), we have demonstrated here that we detect the same general trends with the WFC3 IR grisms using only two orbits of HST time. Future observations of this type will serve to investigate these preliminary trends in a more statistically significant way.

5. Summary

We detect a total of 41 emission lines from 25 galaxies in the ERS II grism field, allowing calculation of line fluxes, SFRs, and grism–spectroscopic redshifts. Thirteen of these galaxies had emission lines in the optical ACS G800L grism data and twelve are newly-detected star–forming galaxies with emission lines in the infrared. We show the SFRs of these galaxies as

a function of redshift and discuss various SFR indicators. We show that the sSFRs of the most massive ($M>10^{11}M_{\odot}$) ELGs are generally lower than their lower mass counterparts, in agreement with recent studies by Zheng et al. (2007) and Damen et al. (2009). These data demonstrate the effieciency of the WFC3 grisms in detecting star–forming galaxies at $z\sim0.2$–2.0. This work sets the stage for larger area and deeper studies of star–forming galaxies with WFC3 in the future, which will serve to greatly increase the sample and statistics and will probe even fainter and less massive sources.

This research was supported in part by an appointment to the NASA Postdoctoral Program at Goddard Space Flight Center, administered by Oak Ridge Associated Universities through a contract with NASA (ANS). This paper is based on Early Release Science observations made by the WFC3 Scientific Oversight Committee. We are grateful to the Director of the Space Telescope Science Institute for awarding Director's Discretionary time for this program. Support for program #11359 was provided by NASA through a grant from the Space Telescope Science Institute, which is operated by the Association of Universities for Research in Astronomy, Inc., under NASA contract NAS 5–26555.

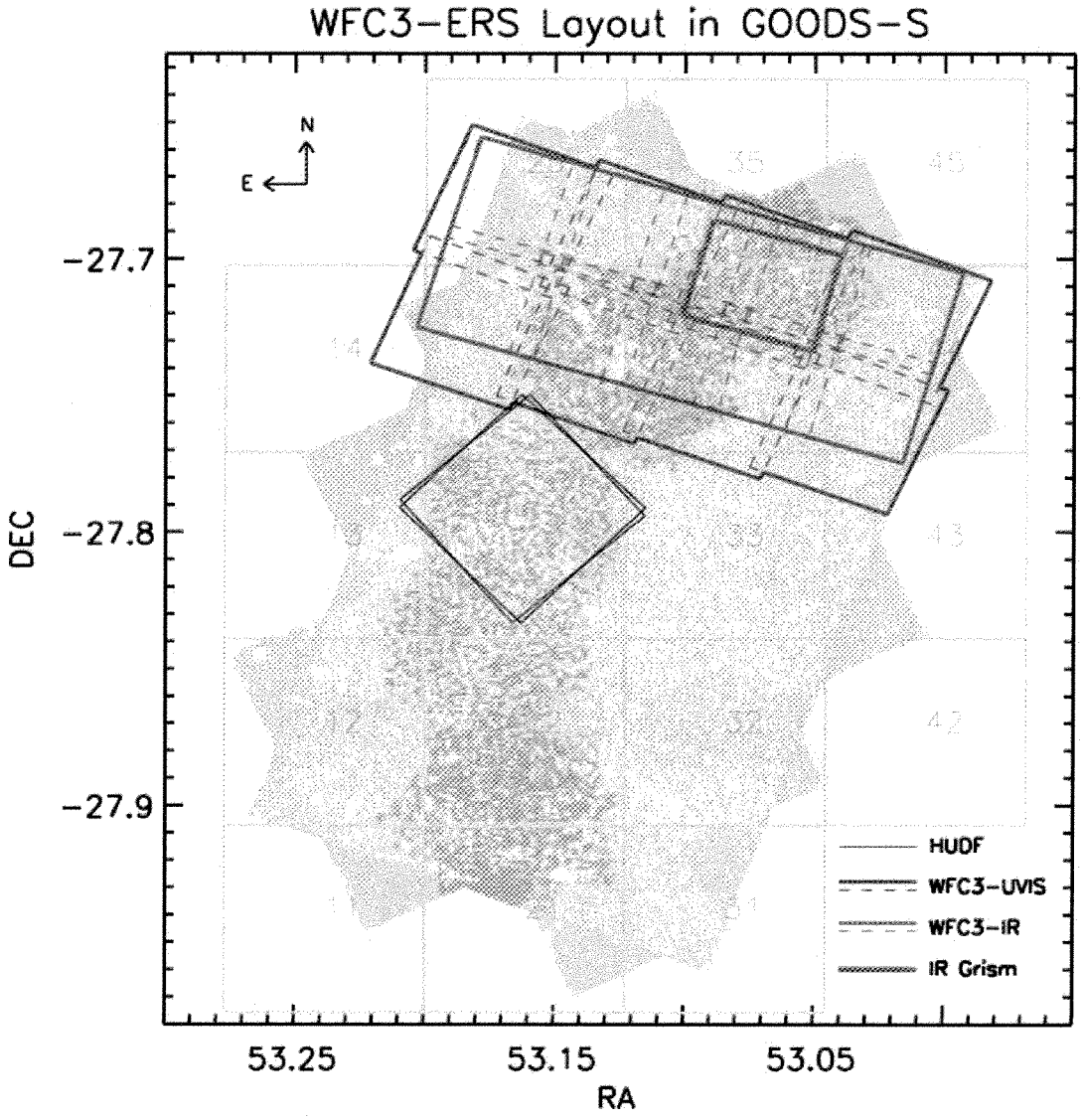

Fig. 1.— ERS II Layout in GOODS–South. Grey area is ACS GOODS–South with tile numbers for that dataset. Yellow areas are the five ACS PEARS grism fields; the black box is ACS HUDF. The WFC3 ERS II UVIS fields are outlined in blue, and WFC3 ERS II IR fields are outlined in red. The green box is the WFC3 ERS II IR grism field.

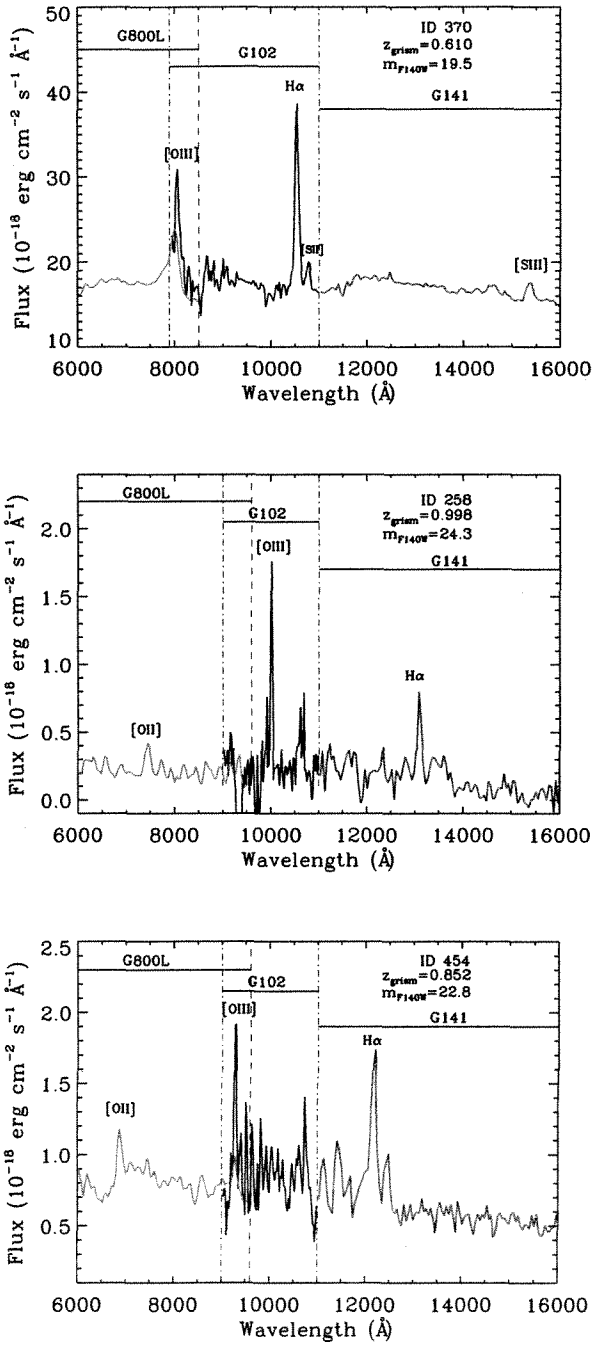

Fig. 2.— Three example grism spectra for ELGs (Table 1 Objects 176308, 119213, 199380 from top to bottom) pre–selected from the ACS PEARS grism ELG study of Straughn et al. (2009). Compared to ACS G800L, the higher–resolution WFC3 grisms allow detection of the [S II] and [S III] lines, and also are able to resolve the [O III] $\lambda\lambda$4959Å, 5007Å lines (middle panel), which are blended in the G800L data.

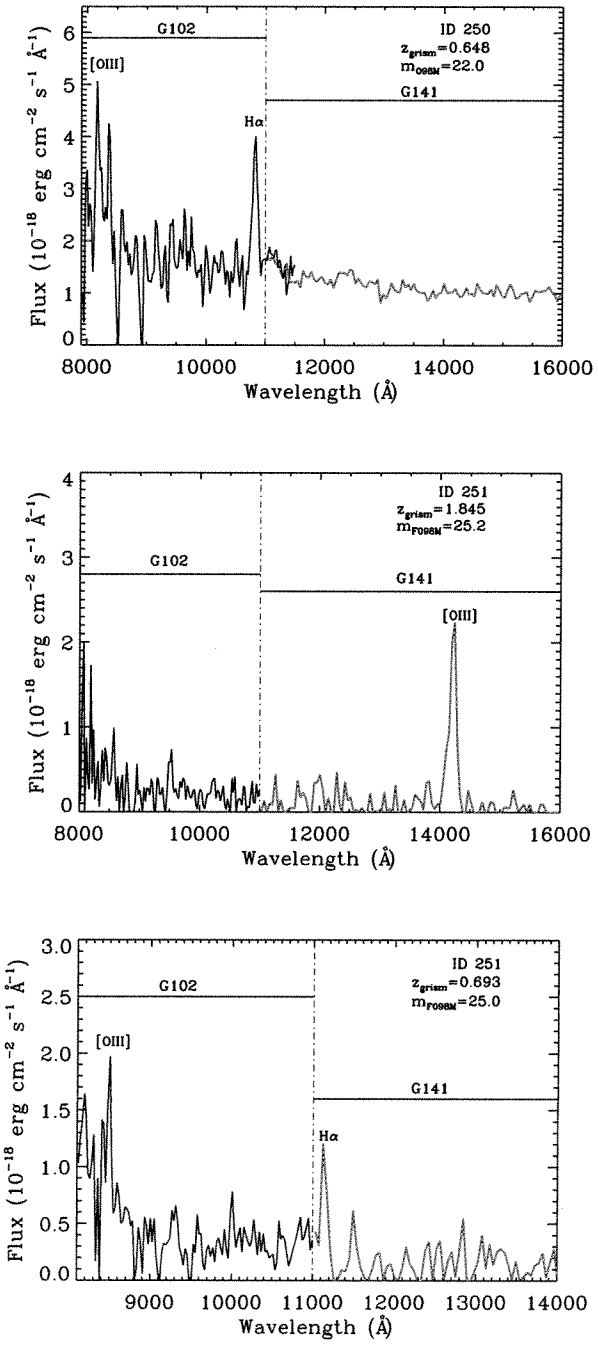

Fig. 3.— Three example grism spectra for ELGs with detected emission lines only in the IR grisms. The 12 ELGs with lines only in the IR have an average continuum magnitude of $AB(F098M)$ =22.8 mag and an average redshift of 1.27.

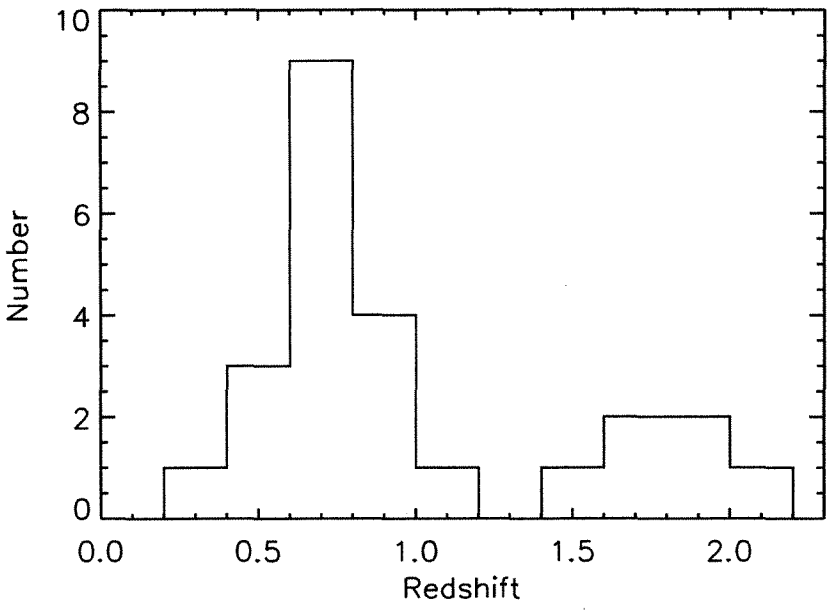

Fig. 4.— Grism redshift distribution of WFC3 ELGs. The Hα [O III] and [O II] emission lines are visible in the WFC grisms at redshifts $0.2 \lesssim z \lesssim 1.6$, $1.2 \lesssim z \lesssim 2.4$ and $2.0 \lesssim z \lesssim 3.6$ respectively.

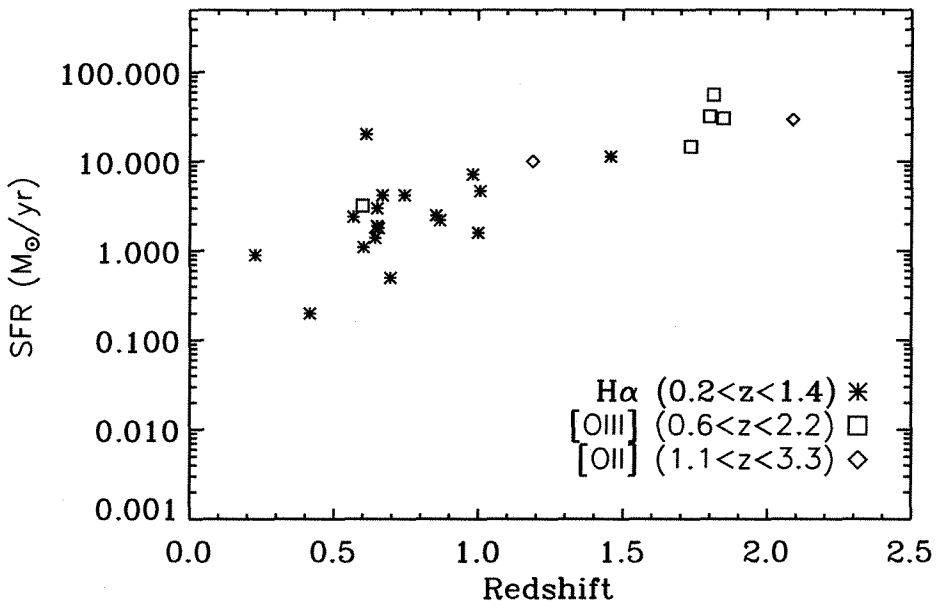

Fig. 5.— Star–formation rate for grism–detected sources as a function of redshift. SFRs are calculated from Hα, [O II], and [O III] in order of preference, as described in Section 4.3

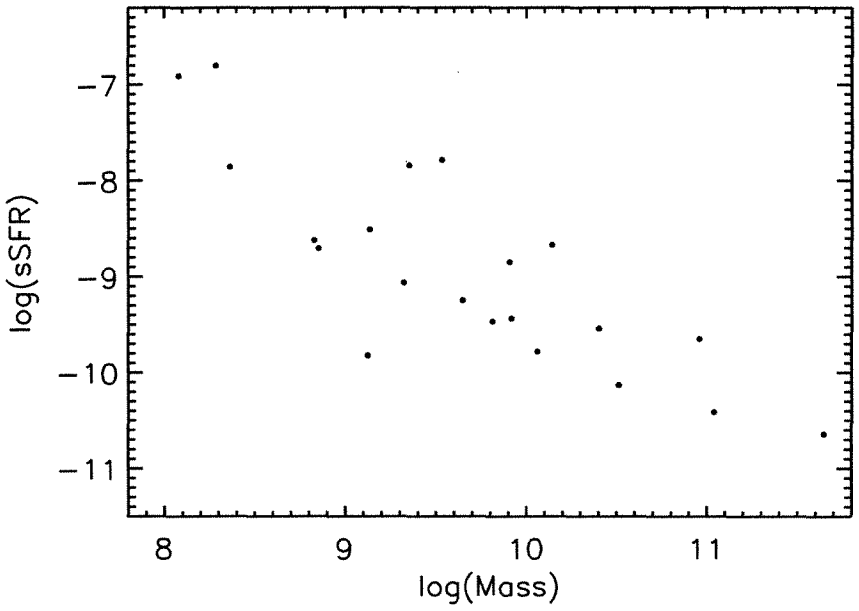

Fig. 6.— Specific star–formation rate as a function of stellar mass, showing the expected relation of lower sSFR at higher mass.

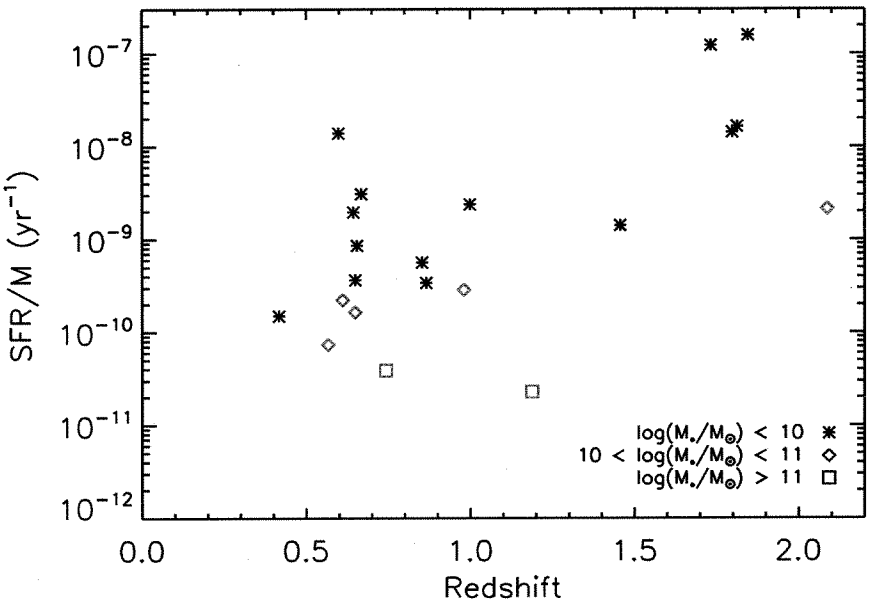

Fig. 7.— Specific star–formation rate as a function of redshift for three different mass bins. Although our sample size is small, we are able to detect the general trend of lower SSFRs for the highest mass galaxies in the 2–orbit grism data.

Table 1. Global Properties of Emission–Line Galaxies

ID –	RA (deg)	Dec (deg)	$AB(F098M)$ (mag)	Wavelength (Å)	Flux ($10^{-18} erg/s/cm^2$)	EW (Å)	Line ID	Grism Redshift	Flag –
242	53.0821381	-27.7137566	24.61	11501	66.1±9.4	69	[O II]	2.071	1
242	53.0821381	-27.7137566	24.61	15337	65.9±6.2	91	[O III]	2.071	1
251	53.0767975	-27.7144318	25.20	14212	98.5±5.1	148	[O III]	1.845	1
262	53.0559158	-27.7187958	25.63	13646	55.8±3.7	140	[O III]	1.732	3
397	53.0772285	-27.7047749	26.86	13821	96.7±43.0	123	–	–	–
418	53.0848618	-27.7014732	24.92	14046	189.7±9.0	124	[O III]	1.812	3
111	53.0628166	-27.7264595	22.44	11055	101.6±1.2	21	[O III]	1.187	1
111	53.0628166	-27.7264595	22.44	8152	90.1±54.3	18	[O II]	1.187	1
193	53.0722466	-27.7189407	20.98	10815	133.9±33.3	36	Hα	0.648	1
210	53.0735207	-27.7174015	22.70	10846	123.2±16.3	72	Hα	0.653	1
211	53.0714264	-27.7175808	20.40	10280	232.1±11.9	21	Hα	0.566	1
215	53.0703049	-27.7178516	23.46	10935	276.5±11.5	25	Hα	0.666	1
600	53.0569191	-27.7202988	22.85	16116	108.6±10.8	377	Hα	1.456	2
250	53.0734177	-27.7159576	22.03	10818	211.3±15.7	69	Hα	0.648	1
258	53.0857010	-27.7113400	24.32	9998	98.7±21.7	125	[O III]	1.002	1
258	53.0857010	-27.7113400	24.32	13110	38.2±7.8	75	Hα	0.998	1
700	53.0565033	-27.7156715	23.42	13167	113.4±8.3	122	Hα	1.006	2
336	53.0577469	-27.7135906	20.71	8685	234.9±38.5	47	[O III]	0.742	1
336	53.0577469	-27.7135906	20.71	11431	213.5±17.8	45	Hα	0.742	1
336	53.0577469	-27.7135906	20.71	11703	64.6±20.0	16	[S II]	0.742	1
336	53.0577469	-27.7135906	20.71	15745	35.6±8.4	10	[S III]λ9069	0.742	1
336	53.0577469	-27.7135906	20.71	16549	61.8±8.4	17	[S III]λ9532	0.742	1
337	53.0656853	-27.7118473	23.88	7975	169.7±14.9	73	[O III]	0.597	1
339	53.0773964	-27.7081947	22.65	10511	95.2±6.5	37	Hα	0.602	1
339	53.0773964	-27.7081947	22.65	8007	650.1±44.2	129	[O III]	0.602	1
364	53.0693626	-27.7090931	23.52	10775	99.6±6.1	71	Hα	0.642	1
364	53.0693626	-27.7090931	23.52	8218	346.6±21.2	152	[O III]	0.642	1
370	53.0551414	-27.7113743	19.51	10565	1660.6±14.5	60	Hα	0.610	1
370	53.0551414	-27.7113743	19.51	8084	905.6±75.6	38	[O III]	0.610	1
370	53.0551414	-27.7113743	19.51	10810	334.5±14.5	20	[S II]	0.610	1
370	53.0551414	-27.7113743	19.51	15354	276.6±11.7	23	[S III]λ9532	0.610	1
370	53.0551414	-27.7113743	19.51	14618	125.7±18.7	10	[S III]λ9069	0.610	1
800	53.0856094	-27.6999264	24.38	13970	111.0±15.9	159	[O III]	1.797	3
427	53.0643578	-27.7057133	22.48	9293	47.6±9.0	25	Hα	0.416	1

REFERENCES

Beckwith, S.V.W. et al. 2006, AJ, 132, 1729

Bertin, E. & Arnouts, S. 1996, A&AS, 117, 363

Bouwens, R.J. et al. 2010, ApJL, 709, 133MNRAS, 351, 1151

Damen, M., Labb, I., Franx, M., van Dokkum, P. G., Taylor, E. N., Gawiser, E. J. 2009, ApJ, 690, 937

Dickinson, M., et al. 2003, Proc. ESO/USM Workshop, "The Mass in Galaxies at Low and High Redshift", ed. R. Bender, & A. Renzini (Berlin: Springer), 324

Fazio, G. G., et al. 2004, ApJS, 154, 10

Gallego, J., Zamorano, J., Aragon-Salamanca, A., & Rego,M. 1995, ApJ 455, L1

Gardner, J.P., et al. 2006, SSR, 123, 485

Giavalisco, M. et al. 2004, ApJL, 600, 93

Grazian, A., et al. 2006, A&A 449, 951

Grogin, N.A., Malhotra, S., Rhoads, J., Cohen, S., Hathi, N., Windhorst, R., Pirzkal, N. 2007, BAAS, 211, 4605

Kennicutt, R.C.,Jr. 1983, ApJ 272, 54

—— 1992, ApJ, 388, 310

—— 1998, ARA&A 36, 189

Kennicutt, R.C., Jr., Bresolin, F., French, H., & Martin, P. 2000, ApJ, 537, 589

Kewley, L.J., Geller, M.J., Jansen, R.A. 2004, AJ, 127, 2002

Koekemoer, A. M., Fruchter, A. S., Hook, R. N., & Hack, W. 2002, The 2002 HST Calibration Workshop, ed. S. Arribas, A. Koekemoer, and B. Whitmore (Baltimore:STScI), 337

Kümmel, M., Walsh, J. R., Pirzkal, N., Kuntschner, H., & Pasquali, A. 2009, PASP, 121, 59

H. Kuntschner, H. Bushouse, M. Kuemmel, J. R. Walsh 2009a, ST-ECF ISR WFC3-2009-18 WFC3 SMOV proposal 11552: Calibration of the G102 grism

Table 1—Continued

ID –	RA (deg)	Dec (deg)	$AB(F098M)$ (mag)	Wavelength (Å)	Flux ($10^{-18} erg/s/cm^2$)	EW (Å)	Line ID	Grism Redshift	Flag –
454	53.0761375	-27.7011642	22.76	9264	62.2±18.9	27	[O III]	0.855	1
454	53.0761375	-27.7011642	22.76	12157	91.2±7.2	64	Hα	0.855	1
498	53.0789032	-27.6977596	21.52	12996	183.5±15.9	58	Hα	0.980	1
559	53.0613899	-27.6981373	21.81	9317	47.1±3.2	14	Hα	0.865	1
246	53.0700302	-27.7166138	24.95	8489	55.9±3.2	50	[O III]	0.693	1
246	53.0700302	-27.7166138	24.95	11113	29.3±3.2	33	Hα	0.693	1
3	53.0825119	-27.6896687	18.67	8056	733.2±3.2	26	Hα	0.227	1

*NOTE: No data indicates measurement was not possible. In the case of line IDs, no data indicates that no suitable line ID was found for the given input redshift. "Grism Redshift" column gives re–calculated redshift based on the line identification. "Flag" column gives source of input redshift used for line identification, where used: 1—two lines visible in spectrum, no prior redshift needed; 2—single line in spectrum, line ID and grism redshift based on prior spectroscopic redshift; 3—single line in spectrum, line ID and grism redshift based on prior photometric redshift.

—— 2009b, ST-ECF ISR WFC3-2009-17 WFC3 SMOV proposal 11552: Calibration of the G141 grism

Larson, R.B. & Tinsley, B.M. 1978, ApJ 219, 46

Li et al. 2008, MNRAS,385, 1903L

Martin, D. C., et al. 2007, ApJS, 173, 415

McCarthy, P.J., et al. 1999, ApJ, 520, 548

McLure, R. J., Dunlop, J. S., Cirasuolo, M., Koekemoer, A. M., Sabbi, E., Stark, D. P., Targett, T. A., Ellis, R. S. 2010, MNRAS, 403, 960

Navarro, J., Frenk, C., & White, S. 1997, ApJ, 490, 493

Oesch, P. A., Bouwens, R. J., Carollo, C. M., Illingworth, G. D., Trenti, M., Stiavelli, M., Magee, D., Labb, I., Franx, M. 2010, ApJL, 709, 21

Overzier, R.A. et al. 2008, ApJ, 677, 37

Perez-Gonzalez, P. G., et al. 2008, ApJ, 675, 234

—— 2006, ApJ 636, 582

Rodighiero, G. et al. 2010, A&A in press (arXiv:1005:1089)

Rosa, M., Joubert, M., Benvenuti, P. 1984, A&AS, 57, 361

Straughn, A.N. et al. 2008, AJ, 135, 1624

Straughn, A.N. et al. 2009, AJ, 138, 1022

van Dokkum, P.G & Brammer, G. 2010, arXiv:1003:3446

White, S. D. M., & Frenk, C. S. 1991, ApJ, 379, 52

Wilkins, S. M., Bunker, A. J., Ellis, R. S., Stark, D., Stanway, E. R., Chiu, K., Lorenzoni, S., Jarvis, M. J. 2010, MNRAS, 403, 938

Wuyts, S., Labbe, I., Schreiber, N. M. F., et al. 2008, ApJ, 682, 985

Xu, C., et al. 2007, AJ 134, 169

Yan, H. Windhorst, R.A., Hathi, N.P., Cohen, S.H., Ryan, R.E., O'Connell, R., McCarthy, P.J. 2010, ApJ in press (arXiv:0910:0077)

Yan, L., McCarthy, P.J., Freudling, W., Teplitz, H.I., Malumuth, E.M., Weymann, R.J., & Malkan, M.A. 1999, ApJL 519, L47

Zheng, X. Z., Bell, E. F., Papovich, C.,Wolf, C., Meisenheimer, K., Rix, H.-W., Rieke, G, & Somerville, R. 2007, ApJ, 661, 41